International Journal of Nanomedicine

Dovepress
open access to scientific and medical research

Open Access Full Text Article

ORIGINAL RESEARCH

Oxygen and indocyanine green loaded phase-transition nanoparticle-mediated photo-sonodynamic cytotoxic effects on rheumatoid arthritis fibroblast-like synoviocytes

This article was published in the following Dove Press journal:
International Journal of Nanomedicine
9 January 2017
Number of times this article has been viewed

Qin Tang[1–3]
Jianyu Cui[1]
Zhonghua Tian[1]
Jiangchuan Sun[4]
Zhigang Wang[2]
Shufang Chang[4]
Shenyin Zhu[1]

[1]Department of Pharmacy, First Affiliated Hospital of Chongqing Medical University, [2]Department of Ultrasound, Institute of Ultrasound Imaging, Second Affiliated Hospital of Chongqing Medical University, [3]State Key Laboratory of Ultrasound Engineering in Medicine Co-founded by Chongqing and the Ministry of Science and Technology, [4]Department of Obstetrics and Gynecology, Second Affiliated Hospital of Chongqing Medical University, Chongqing, People's Republic of China

Correspondence: Shenyin Zhu; Shufang Chang
Department of Pharmacy, First Affiliated Hospital of Chongqing Medical University, No 1, Yixueyuan Road, Yuzhong District, Chongqing 400016, People's Republic of China
Tel +86 23 8901 2401
Fax +86 23 6881 1793
Email zhushenyin0486@sina.com; shfch2005@163.com

Background: Photodynamic therapy and sonodynamic therapy are developing, minimally invasive, and site-specific modalities for cancer therapy. A combined strategy PSDT (photodynamic therapy followed by sonodynamic therapy) has been proposed in this study. Here, we aimed to develop novel biodegradable poly(DL-lactide-*co*-glycolic acid) phase-transition nanoparticles simultaneously loaded with oxygen and indocyanine green (OI-NPs) and to investigate the cytotoxic effects and the potential mechanisms of OI-NP–mediated PSDT on MH7A synoviocytes.

Methods: The OI-NPs were prepared using a modified double emulsion method and the physicochemical properties were determined. The cellular uptake of OI-NPs was detected by confocal microscopy and flow cytometry. 3-(4,5-Dimethylthiazol-2-yl)-2,5-diphenyltetrazoliumbromide assay, flow cytometry, and Hoechst 33342/propidium iodide double staining were used to determine the cytotoxic effect of OI-NP–mediated PSDT on MH7A cells. Fluorescence microscope and fluorescence microplate reader were used to detect reactive oxygen species (ROS) generation.

Results: The OI-NPs were a stable and efficient carrier to deliver oxygen and indocyanine green, and enhanced cellular uptake was observed in MH7A cells with the nanoparticles. OI-NP–mediated PSDT caused more serious cell damage and more evident cell apoptosis, compared with other groups. Furthermore, increased generation of intracellular ROS was detected in MH7A cells treated with PSDT. Interestingly, the OI-NP–mediated PSDT-induced cell viability loss was effectively rescued by pretreatment with the ROS scavenger *N*-acetylcysteine.

Conclusion: Multifunctional OI-NPs were successfully developed and characterized for the combined delivery of oxygen and indocyanine green, and OI-NP–mediated PSDT would be a potential cytotoxic treatment for MH7A cells. This study may provide a novel strategy for the treatment of RA and develop a model of theranostic application through phase-transition nanoparticle-mediated PSDT in the future.

Keywords: multifunctional nanoparticles, indocyanine green, synoviocytes, reactive oxygen species, apoptosis

Introduction

Rheumatoid arthritis (RA) is a chronic systemic autoimmune disease of uncertain cause that is associated with progressive disability, systemic complications, and socioeconomic costs, with approximately 1% of the adult population affected worldwide.[1–3] It characteristically involves the small joints in a symmetric pattern with a potential for progressive joint destruction, and extra-articular and systemic features may also be present.[1]

submit your manuscript | www.dovepress.com
Dovepress
http://dx.doi.org/10.2147/IJN.S120902

Similar to a locally invasive tumor, abnormal synovium proliferation and local hypoxia of the involved joint play important roles in the pathogenesis of RA. In this process, RA fibroblast-like synoviocytes (RA-FLSs) play key roles by producing cytokines and proteases that perpetuate inflammation and contribute to cartilage destruction. Besides, it increases invasiveness into the extracellular matrix by developing a unique aggressive phenotype, which further exacerbates joint damage.[4] Furthermore, the excessive proliferation of FLSs in RA synovium leads to increased oxygen consumption and local microenvironment hypoxia, which contribute to synovium inflammation, proinflammatory cell infiltration, angiogenesis, and cartilage degradation.[5] The above processes promote mutually, form a positive feedback loop, and jointly promote the progression of RA. Despite some impressive advances in the proapoptosis effects for FLSs, most of these therapies involved are nontargeted or have limited efficacy.[4–6] In addition, little research has been done on improving the local hypoxia to increase the effect of RA treatment. Therefore, in this study, we have used a promising strategy for the treatment of RA, which aims simultaneously at inducing FLSs apoptosis and improving the local hypoxia microenvironment.

Photodynamic therapy (PDT) is a clinically approved therapeutic modality that can exert a minimally invasive and site-selective cytotoxic effect toward many proliferative diseases.[7] It has been proposed and experimentally studied as a new RA synovectomy modality in the last few years.[8–10] However, limited penetrating ability of light is one of the reasons hampering further study of PDT-mediated therapeutic effect on RA. Compared with the light used in PDT, ultrasound has better penetrability, which can easily act on the lesion at a deep site.[11,12] Besides, it is currently believed that the combination of PDT and sonodynamic therapy (SDT) may decrease the sensitizer dosage and ultrasound/light energy, which can further reduce the side effects, while enhancing the curative effect dramatically.[13–17] Thus, PDT combined with SDT (PSDT) is considered for the lesion of deep site in the present study. The underlying mechanisms of PDT and SDT are quite different, and the mechanisms of PSDT are very complicated. However, generation of reactive oxygen species (ROS) is believed to be one of the primary cytotoxicity mechanisms by which cell apoptosis or necrosis is induced.[13,14,18–21]

Indocyanine green (ICG) is a water-soluble tricarbocyanine dye that strongly absorbs in near-infrared region.[22–24] Studies have demonstrated that ICG can be activated by both light and ultrasound.[25] However, the applications of ICG are mainly hindered by some characteristics, including instability (aqueous instability, thermal degradation, and photodegradation), high protein binding (which leads to its rapid elimination from the body), lack of targeting, and its proneness to photobleaching.[26–28] An investigation of the new nanotechnology and drug delivery systems would bring hope to overcome these restrictions. In recent years, poly(DL-lactide-*co*-glycolic acid [PLGA]) has been widely used in medical and biologic applications for its biodegradability, biocompatibility, safety, and stability.[29–32] Several studies have demonstrated that ICG-loaded PLGA nanoparticles (NPs) could improve the stability of ICG and act as an efficient carrier to deliver ICG to the lesion area to perform the function of therapy or imaging.[33–36] Furthermore, it has been demonstrated that liquid perfluorocarbon compounds (PFC) act as a good oxygen carrier[37] and are widely used in ultrasound imaging, and PLGA NPs entrapped with PFC droplets have been reported in several studies.[38–40] So far, there is no report about the establishment and application of PLGA NPs delivering ICG and oxygen simultaneously.

In this study, we aimed to develop a novel nanoscale PLGA drug delivery system which encapsulates oxygen-saturated perfluoro-*n*-pentane (PFP) and ICG, and to investigate the cytotoxic effects of OI-NP–mediated PSDT against FLSs and the potential mechanisms involved in vitro. The in vitro study will pave the way for future in-depth in vivo study of OI-NP–mediated PSDT on RA. To our knowledge, this is the first study to successfully develop ICG and oxygen-loaded PLGA nanosystem and the first attempt to apply PSDT-mediated cytotoxic effects on synoviocytes for the treatment of RA.

Materials and methods

Chemicals and reagents

ICG was purchased from Sigma-Aldrich Co. (St Louis, MO, USA). PLGA (lactide:glycolide =50:50, molecular weight =12,000 Da) was obtained from the Shan-dong Key Laboratory of Medical Polymer Materials (Shandong, People's Republic of China). PFP (a PFC compound with a boiling point of 29°C) was obtained from Fluka (St Louis, MO, USA). Polyvinyl alcohol (PVA, 87%–90%) was also obtained from Sigma-Aldrich Co. Singlet oxygen Sensor Green (SOSG) was purchased from Thermo Fisher Scientific (Waltham, MA, USA). Hoechst 33342/propidium iodide (HO/PI) double-staining kit was obtained from Nanjing Jiancheng Bioengineering Institute (Nanjing,

People's Republic of China). 2-(4-amidinophenyl)-6-indolecarbamidine dihydrochloride (DAPI), *N*-acetylcysteine (NAC), 3-(4,5-dimethylthiazol-2-yl)-2,5-diphenyltetrazolium bromide (MTT), and 2′,7′-dichlorofluorescin diacetate (DCFH-DA) were all supplied by Beyotime Biotechnology (Shanghai, People's Republic of China). All other reagents used in this study were commercial products of analytical grade. Ultrapure water (EMD Millipore, Billerica, MA, USA) was used to prepare all solutions.

Preparation of OI-NPs

OI-NPs were prepared using a modified double emulsion method adapted from previously published studies.[29,41] 1) 25 mg/mL PLGA solution in methylene chloride and 2 mg/mL ICG solution in water were prepared in advance and PVA was dissolved in water to form 5% w/v aqueous solution. 2) 200 µL PFP was bubbled with oxygen gas till saturation and added to ICG aqueous solution and the mixture was subjected to vibration for 1 min using an ultrasonic probe (Sonics & Materials, Inc., Fairfield, CT, USA). Then, the uniform mixture was bubbled with oxygen again for 2 min. Subsequently, the PLGA solution was added to the mixture and sonicated by the ultrasonic probe at 100 W for 2 min to form an initial emulsion. 3) The emulsion was added to the 5% PVA aqueous solution and sonicated again to produce the second emulsion. Then, the emulsion was stirred for 4 h to extract methylene chloride sufficiently. Also, the solution was centrifuged (5806 R; Eppendorf, Hamburg, Germany) at 12,000 rpm for 8 min at 4°C and the supernatant was discarded. The precipitate was washed by water until the supernatant was clarified. 4) The washed precipitate was resuspended in 3 mL water enriched with oxygen and stored at 4°C for further use. Blank NPs and ICG-loaded NPs (I-NPs) were prepared similarly using water instead of ICG solution and omitting all the oxygen saturation processes. All of the operations were kept on ice and in the dark to prevent evaporation of the PFP and decomposition of the ICG.

Characterization of the OI-NPs

Microscopy imaging and characterization measurement

The morphologic characterization of OI-NPs was imaged by light microscope (Olympus IX53; Olympus, Tokyo, Japan), Scanning Electron Microscope (SEM, Hitachi S-340 0N; Hitachi Ltd., Tokyo, Japan), and Transmission Electron Microscope (TEM, Hitachi H-760 0; Hitachi Ltd.). Size, size distribution, surface zeta potential, and polydispersity index (PDI) of the NPs were determined by dynamic light scattering using a Malvern Zetasizer Nano ZS unit (Malvern Instruments, Malvern, UK) at room temperature.

Determination of ICG entrapment efficiency and loading efficiency

The entrapment efficiency and the content of ICG loaded in NPs were determined in triplicate by an ultraviolet–visible (UV–Vis) spectrophotometer (260-Bio, Thermo Fisher Scientific). The supernatant of centrifugation and washing process was collected and the concentration of ICG in the supernatant was quantified by measuring the absorbance at 780 nm and comparing the reading to a standard concentration curve of free ICG in the same solvent. The entrapment efficiency and the content were calculated as follows: entrapment efficiency (%) = ([ICG used in formulation – ICG in supernatant]/ICG used in formulation) ×100; content (% w/w) = ([ICG used in formulation – ICG in supernatant]/mass of NPs) ×100.

Optical spectra measurement

The absorption spectra of free ICG and OI-NPs were obtained using UV-Vis spectrophotometer (the wavelength was from 550 to 850 nm). The fluorescence spectra were obtained using fluorescence spectrometer (Cary Eclipse, Agilent Technologies) with excitation of 775 nm, and the emission spectra were recorded from 785 to 850 nm. Both excitation slit width and emission slit width were 10 nm. Also, we measured the absorbance at different time intervals to evaluate the stability of the NPs. In brief, the absorbance (at 780 nm) of the samples was detected every 5 days for 40 days by UV–Vis spectrophotometer.

In vitro ICG release study of OI-NPs

The detection procedure was similar to those used in previous studies.[36,42] In brief, the OI-NPs were resuspended in phosphate-buffered saline (PBS, pH 7.4) and sonicated to get a homogenous dispersion. The suspension was divided into aliquots in microcentrifuge tubes and the tubes were placed in an incubator oven at 37°C and a stirring speed of 100 rpm. At an indicated time point, the samples were collected and centrifuged at 10,000 rpm for 6 min. The precipitate was dispersed for the fluorometric assay of the ICG remaining after the release. Release kinetic studies were done up to 48 h. The cumulative percentage of ICG released from the NPs at an indicated time interval was calculated by the following equation: ICG released (%) =100% − ICG remaining (%).

Measurement of ROS generation in cell-free system

The SOSG solution (5 μM) in degassed water was added to the free ICG, I-NPs, or OI-NPs (10 μg/mL of ICG). The solution was irradiated with laser light and then immediately exposed to ultrasound while being kept in the dark (the parameters of laser and ultrasound were consistent with the following experimental part). ROS production before and after the exposure to laser and ultrasound was determined by measuring the fluorescence intensity of SOSG with a fluorescence microplate reader (Varioskan Flash, Thermo Fisher Scientific; Ex =504 nm, Em =525 nm).

Cell culture

Human FLSs MH7A cell line was purchased from RIKEN Bio Resource Center (Ibaraki, Japan). The cells were cultured in Dulbecco's Modified Eagle's Medium containing 15% fetal bovine serum under a humidified atmosphere in 5% CO_2 at 37°C. For all experiments, cells in the exponential phase of growth were used.

Cellular uptake determination

The cellular uptake of OI-NPs was determined by confocal laser scanning microscopy (CLSM; A1+ R; Nikon Corporation, Tokyo, Japan) and flow cytometry (BD Biosciences, San Jose, CA, USA). Briefly, MH7A cells were seeded into a six-well plate (1×10^6 cells/well) and incubated overnight. Then, the medium was changed to serum-free medium containing either free ICG or OI-NPs (10 μg/mL of ICG) and incubated for 4 h. The cells were washed thrice with PBS and harvested for flow cytometry determination or fixed with 4% paraformaldehyde solution for CLSM detection.

Determination of intracellular ROS generation

Intracellular generation of ROS was detected with the fluorescence indicator DCFH-DA. MH7A cells were seeded in 24-well plates (6×10^4 cells/well). After overnight incubation, the medium was replaced with 0.5 mL serum-free medium which contained free ICG, I-NPs, or OI-NPs (10 μg/mL of ICG) and was incubated for 4 h. The cells were washed with PBS to remove the excess NPs, and DCFH-DA (10 μM) was added and incubated for 30 min. Then, the cells were exposed to laser and ultrasound. After incubation for another 30 min, the green fluorescent signal of 2′,7′-dichlorofluorescein, which indicated the generation of reactive oxygen in the cells, was qualitatively imaged using fluorescence microscopy (Eclipse Ti, Nikon Corporation) and quantitatively detected using fluorescence microplate reader.

In vitro experimental protocol

MH7A cells were divided into the following groups: 1) control group (control), 2) PSDT alone (PSDT), 3) OI-NPs alone (OI-NPs), 4) ICG-mediated PSDT (ICG + PSDT), 5) I-NP–mediated PSDT (I-NPs + PSDT), and 6) OI-NP–mediated PSDT (OI-NPs + PSDT). MH7A cells were incubated with free ICG, I-NPs, or OI-NPs containing serum-free medium according to the previous grouping and were incubated at 37°C for 4 h in the dark. Then, the cells were washed thrice slightly using PBS and each well was replaced with complete medium. For PSDT group, an 808 nm diode laser (Mid-River Ltd., Xi'an, People's Republic of China), emitting at 808 nm with a power density of 0.75 W/cm^2, was placed 50 mm upon the medium. Care was taken to ensure that the beam was covering the same field of each well to be treated. Then, the cells were immediately exposed to low-intensity focused ultrasound. The focused ultrasound transducer (25 mm in diameter, 1.0 MHz in frequency), power amplifier, and ultrasonic generator used in this study were assembled by National Engineering Research Centre of Ultrasound Medicine (Chongqing, People's Republic of China). The intensity of 1.0 W/cm^2 and the duration time of 1 min were used. After various treatments, cells were incubated at 37°C in a humidified 5% CO_2 atmosphere for additional time and then subjected to different determinations (MTT assay, flow cytometry analysis and HO/PI double staining).

Cell cytotoxicity assay

The cytotoxicity of different treatments on MH7A cells was evaluated at 24 h posttreatment by MTT assay according to the standard protocol. Cell viability was calculated by the following equation: cell survival (%) = optical density $(OD)_{\text{treatment group}}/OD_{\text{control group}} \times 100\%$. For inhibitory experiment, the ROS scavenger NAC (5 mM) was added to MH7A cells 1 h prior to laser and ultrasound exposure.

Flow cytometry analysis of apoptosis

Apoptosis of MH7A cells was measured using Annexin V-fluorescein isothiocyanate (FITC)/PI double staining and was analyzed by flow cytometry at 24 h after different treatments. Briefly, the cells were seeded at a density of 1×10^6 cells/well in six-well plates. After different treatments for 24 h, the cells were stained with an Annexin V-FITC/PI apoptosis kit following the manufacturer's instructions. After incubation for 15 min at room temperature in the dark, the cells were analyzed by flow cytometer.

Nuclear morphology study for apoptosis

In this study, HO/PI double staining was used to determine the integrity of cell membrane and the cell apoptotic morphologic characteristics. At 24 h after treatment, MH7A cells were washed with PBS, and then HO and PI were added to the culture medium according to the standard protocol. After an incubation period of 10 min at 37°C in the dark, the cells were observed under a fluorescence microscope.

Statistical analysis

Statistical analysis of the data was performed using GraphPad Prism 5.0. All data are expressed as mean ± standard deviation (SD). Differences among the groups were analyzed using one-way analysis of variance method. *P*-values <0.05 were considered statistically significant.

Results

Characterization of the OI-NPs

The schematic structure of the prepared OI-NPs is illustrated in Scheme 1. The ICG was encapsulated in the PLGA shell, while oxygen-saturated PFP was wrapped in the core of the NPs. Scheme 2 is a schematic illustration showing the procedure of OI-NP–mediated PSDT.

The physical properties of OI-NPs are presented in Figure 1. The optical microscopy image of the OI-NPs offers a qualitative view of the larger NPs in the samples (Figure 1A). The TEM image of OI-NPs showed that the NPs were generally spherical in shape with good monodispersity (Figure 1B). Also, the SEM analysis showed that the NPs had a smooth surface (Figure 1C). The average diameter of the OI-NPs (by dynamic light scattering measurement) was 277.80±22.49 nm with a PDI of 0.06±0.01 (Figure 1D), and the zeta potential was −20.0±5.45 mV (Figure 1E).

Table 1 shows the results of the entrapment efficiency and the loading efficiency of ICG in the OI-NPs (56.63%±8.60% and 1.15%±0.16%, respectively). Besides, size distribution, PDI, zeta potential, entrapment efficiency, and loading content of blank NPs, I-NPs, and OI-NPs were compared in this study. The results showed that the differences were not statistically significant.

The optical properties of OI-NPs were also detected. As shown in Figure 2, the absorption and emission peaks of OI-NPs were red-shifted approximately 30 and 10 nm, respectively, compared with those of free ICG (Figure 2A and B). The absorption spectra of the ICG and OI-NPs at different time intervals were measured to determine whether the NPs have a higher stability than free ICG. The absorbance values of the divided groups were measured continuously until freely ICG was almost completely degraded (Figure 2C), while the OI-NPs only experienced a slight decreased of absorbance after 40 days (Figure 2D).

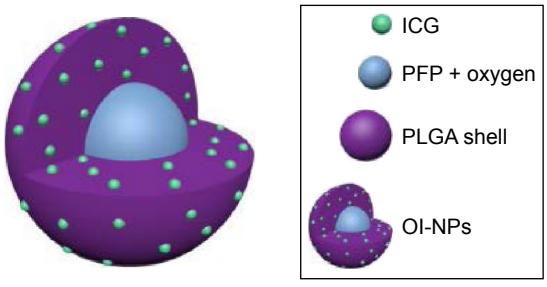

Scheme 1 Schematic illustration of the structure of OI-NPs.
Abbreviations: ICG, indocyanine green; OI-NPs, oxygen and indocyanine green loaded nanoparticles; PFP, perfluoro-*n*-pentane; PLGA, poly(DL-lactide-*co*-glycolic acid).

Release profile of ICG from OI-NPs and ROS generation in cell-free system

The release profile of ICG from the NPs is shown in Figure 3A. The results suggest the accumulative release pattern of ICG from the NPs was exponential, which was consistent with the reported studies.[36,42] Drug release occurs in two phases: an initial "burst" release phase and subsequent slower release. ICG showed a 60% accumulative release after 12 h and a slower release process was noted thereafter. The mean accumulative release of ICG was 71.34% until 24 h, and up to 48 h, the accumulative release of ICG was only increased by 4.15%.

To determine the ROS production of the OI-NPs upon exposure to laser and ultrasound, the amount of generated ROS in degassed water was evaluated using SOSG as an indicator. As shown in Figure 3B, a plot of percentage increase in fluorescent intensity of SOSG before and after laser and ultrasound treatment for ICG, I-NPs, and OI-NPs was constructed. However, the fluorescence intensity of OI-NP–mediated PSDT group was significantly increased (286.46%±51.35%) compared with those of ICG- and I-NP–mediated PSDT groups (201.26%±20.85% and 184.87%±41.73%, respectively). Also, no distinct fluorescence intensity increase was detected by adding the ROS scavenger NAC in advance, indicating that OI-NP–mediated PSDT was indeed capable of producing ROS.

Cellular uptake and intracellular ROS production

The cell uptake behavior of free ICG and OI-NPs was investigated using CLSM and flow cytometry (Figure 4A and B). Figure 4A clearly demonstrates that the cells incubated with

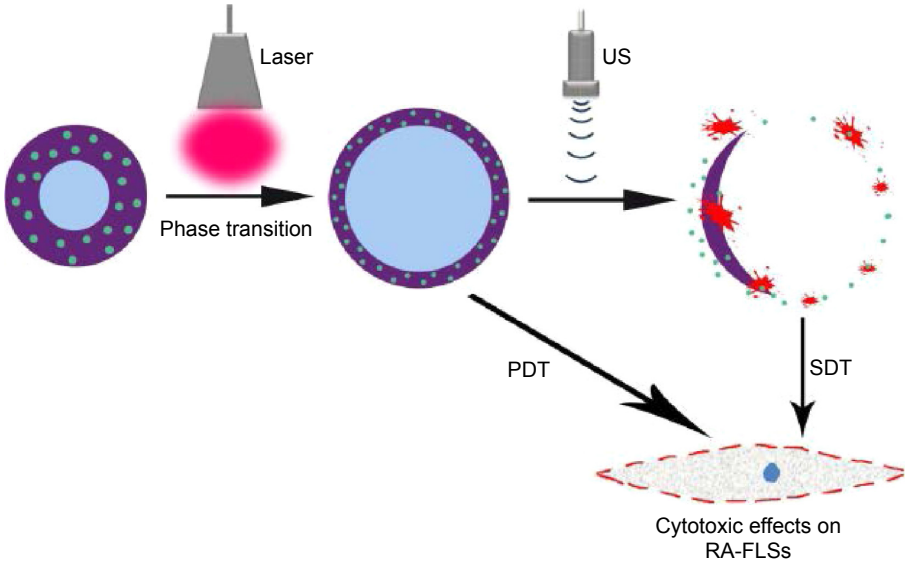

Scheme 2 Schematic illustration of the structure of OI-NP–mediated PSDT for MH7A cells. Liquid-gas transition and photodynamic reaction occurred in the OI-NPs under laser irradiation. The phase-transited OI-NPs were ruptured when exposed to low-intensity focused ultrasound and it caused a sonodynamic reaction.
Abbreviations: OI-NPs, oxygen and indocyanine green loaded nanoparticles; PDT, photodynamic therapy; RA-FLSs, rheumatoid arthritis fibroblast-like synoviocytes; SDT, sonodynamic therapy; US, ultrasound.

OI-NPs exhibited much stronger intracellular fluorescence signals in the cytoplasm, compared to the cells incubated with free ICG. Figure 4B shows the quantitative results detected by flow cytometry. The quantitative results show that the average fluorescence intensity was 16-fold greater in OI-NPs group (40.64%) than that in free ICG group (2.58%), which further demonstrates that the encapsulation of ICG in PLGA NPs could improve the cell uptake ability.

The intracellular generation of ROS was observed by fluorescence microscope and fluorescence microplate reader (Figure 5). No obvious green fluorescence was detected in the control group (2.78±1.17). However, cells treated with free

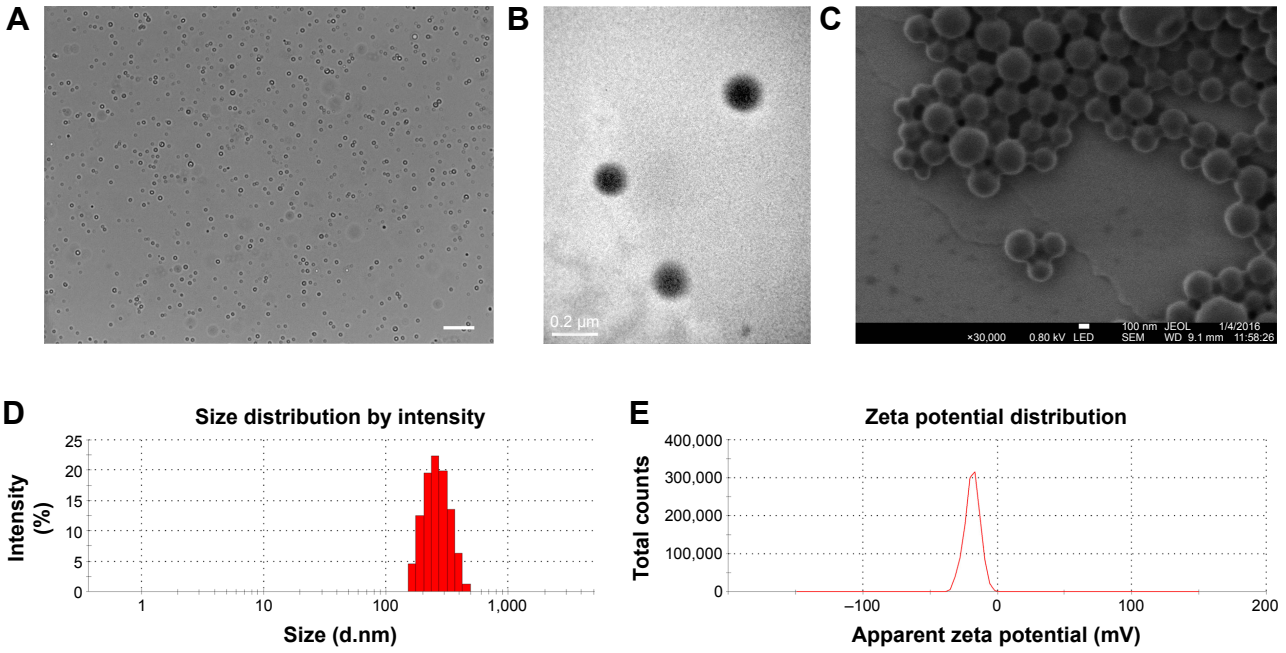

Figure 1 The characterization of OI-NPs.
Notes: (**A**) Optical microscopy images of OI-NPs, scale bar is 10 μm. (**B**) TEM image of OI-NPs. (**C**) SEM image of OI-NPs. (**D**) Size distribution of OI-NPs by DLS measurement. (**E**) The zeta potential of OI-NPs measured by DLS.
Abbreviations: DLS, dynamic light scattering; OI-NPs, oxygen and indocyanine green loaded nanoparticles; SEM, scanning electron microscopy; TEM, transmission electron microscopy.

Table 1 Physicochemical property of the developed nanoparticles

Groups	Size distribution (nm)	PDI	Zeta potential (mV)	Encapsulation efficiency (%)	ICG loading (%)
Blank NPs	264.03±23.13	0.06±0.03	−19.33±4.22	–	–
I-NPs	262.90±12.37	0.08±0.10	−20.77±3.78	58.85±5.53	1.18±0.11
OI-NPs	277.80±22.49	0.06±0.01	−20.00±5.45	56.63±8.60	1.15±0.16

Notes: No significant differences were found among the three groups. Values represent the mean ± SD (n=3).
Abbreviations: ICG, indocyanine green; I-NPs, indocyanine green loaded nanoparticles; NPs, nanoparticles; OI-NPs, oxygen and indocyanine green loaded nanoparticles; PDI, polydispersity index; SD, standard deviation.

ICG, I-NPs, or OI-NPs and then exposed to laser and ultrasound showed enhanced intracellular green fluorescence; especially, the I-NP– or OI-NP–mediated PSDT groups displayed the strongest intracellular fluorescence in MH7A cells ($P<0.001$ and $P<0.001$ vs control and ICG-mediated PSDT group, respectively). Besides, the OI-NP–mediated PSDT group pretreated with NAC displayed no obvious fluorescence.

Cytotoxic effects with OI-NP–mediated PSDT

As shown in Figure 6A, no obvious cytotoxicity against MH7A cells was noted in the free ICG group, even if the concentration was increased up to 100 μg/mL. In contrast, the OI-NPs caused significant cytotoxicity against MH7A cells when the ICG content was >10 μg/mL. An ICG concentration of 10 μg/mL (both for OI-NPs and free ICG) was used in the following studies.

Figure 6C shows the cytotoxic effects on MH7A cells under different treatments. No obvious cytotoxicity was observed in PSDT or blank NP-mediated PSDT group (93.39%±3.93% and 93.17%±1.95% of cell viability, respectively). However, when treated with ICG, I-NPs, or OI-NPs and followed by laser and ultrasound exposure, significant loss in cell viability was observed (75.03%±2.93%, 31.67%±4.28%, and

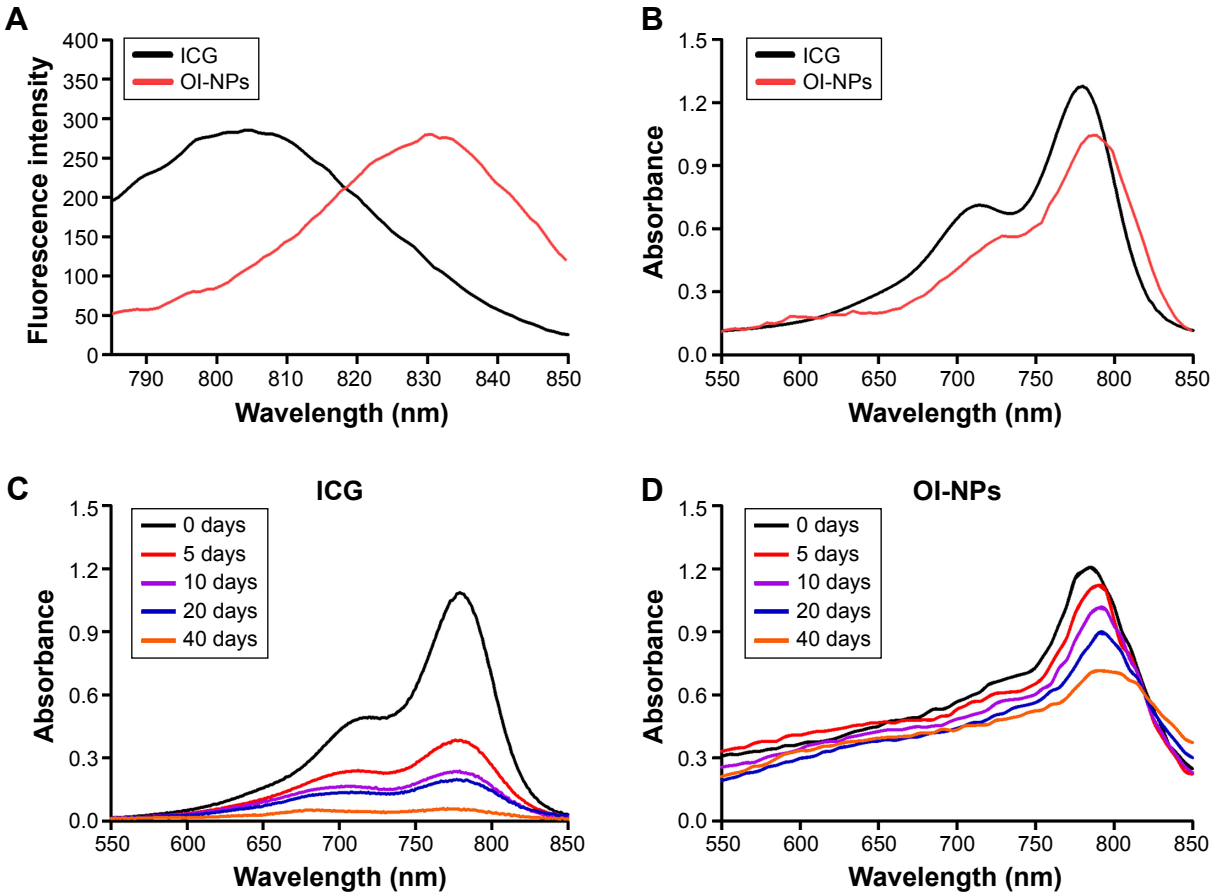

Figure 2 Optical spectra measurement of ICG and OI-NPs.
Notes: Fluorescence (**A**) and absorption (**B**) spectra of free ICG and OI-NPs. The optical stability of free ICG (**C**) and OI-NPs (**D**) at different time intervals. The results demonstrated that OI-NPs had a higher stability compared to freely dissolved ICG.
Abbreviations: ICG, Indocyanine green; OI-NPs, oxygen and indocyanine green loaded nanoparticles.

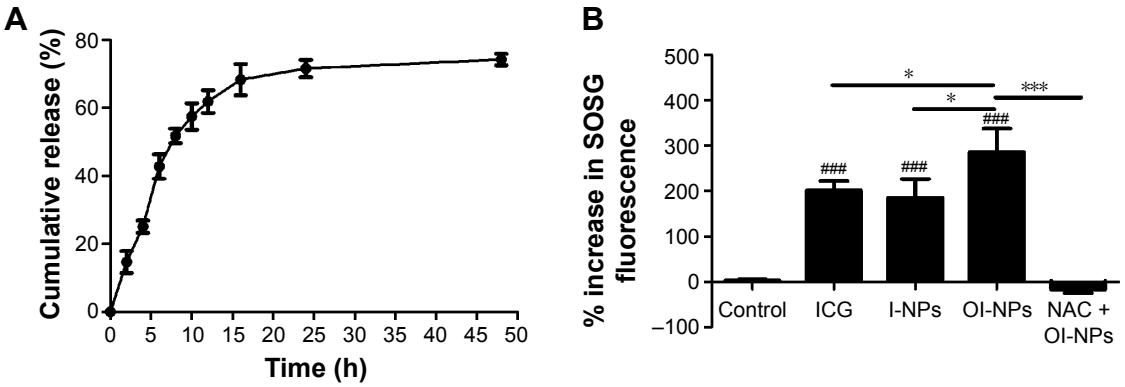

Figure 3 Release profile of ICG from OI-NPs and ROS generation in cell-free system.
Notes: Release profile of ICG from OI-NPs in PBS at 37°C (**A**). Plot of % increase in SOSG fluorescence for ICG, I-NPs, OI-NPs, and NAC plus OI-NPs in degassed water with laser and ultrasound exposure (measured by fluorescence microplate reader) (**B**). Values are mean ± SD (n=3). ###$P<0.001$ versus control group. *$P<0.05$ and ***$P<0.001$ between groups.
Abbreviations: ICG, indocyanine green; I-NPs, ICG-loaded nanoparticles; NAC, *N*-acetylcysteine; OI-NPs, oxygen and indocyanine green loaded nanoparticles; PBS, phosphate-buffered saline; ROS, reactive oxygen species; SD, standard deviation; SOSG, singlet oxygen sensor green.

25.05%±5.42%, respectively) and the cytotoxicity was greater in I-NP– or OI-NP–mediated PSDT group than that in ICG-mediated PSDT group ($P<0.001$). Although the whole cell viability in OI-NP–mediated PSDT group was lower than that in I-NP–mediated PSDT, the difference was not statistically significant ($P>0.05$). To further investigate the role of ROS in cell damage induced by OI-NP–mediated PSDT, cells were pretreated with NAC, and the result showed that the cell viability was significantly increased (75.24%±6.00%, $P<0.001$).

Cell apoptosis induced by different treatments

The cytotoxic effect of PSDT on MH7A cells was further quantified by flow cytometry and qualified by fluorescence microscopy. As shown in Figure 7A–F, the apoptosis efficiencies for the treatment groups A–F are 5.59%±0.36%, 8.94%±0.64%, 6.70%±0.97%, 27.66%±3.24%, 76.44%±6.80%, and 86.23%±12.55%, respectively. It shows that ICG-, I-NP–, or OI-NP–mediated PSDT induced significantly more cell apoptosis as compared with the control group ($P<0.01$, $P<0.001$, and $P<0.001$, respectively). Besides, both I-NP– and OI-NP–mediated PSDT groups could induce higher rate of cell apoptosis than ICG-mediated PSDT group ($P<0.001$). In addition, the apoptosis rate of OI-NP–mediated PSDT group was higher than that of I-NP–mediated PSDT group, but the difference did not show statistical significance ($P>0.05$).

The qualitative study results of inducing cell apoptosis is shown in Figure 7H. Control, PSDT, and OI-NPs

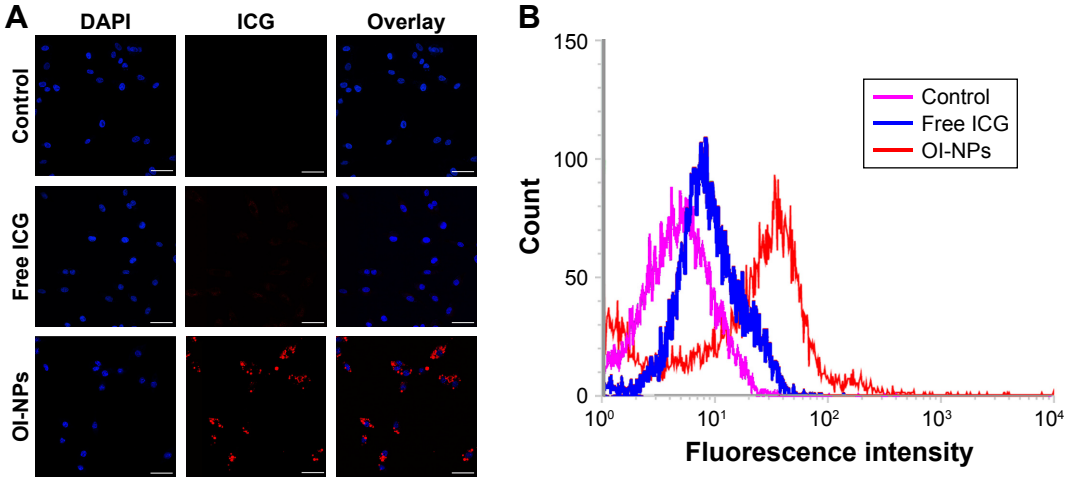

Figure 4 Cellular uptake of free ICG and OI-NPs by MH7A cells.
Notes: CLSM images of MH7A cells subcellular localization (**A**) and flow cytometric analysis of mean fluorescence intensity in MH7A cells incubated with media (pink), free ICG (blue), and OI-NPs (red) for 4 h (**B**). Scale bar is 50 μm.
Abbreviations: CLSM, confocal laser scanning microscopy; DAPI, 2-(4-amidinophenyl)-6-indolecarbamidine dihydrochloride; ICG, indocyanine green; OI-NPs, oxygen and indocyanine green loaded nanoparticles.

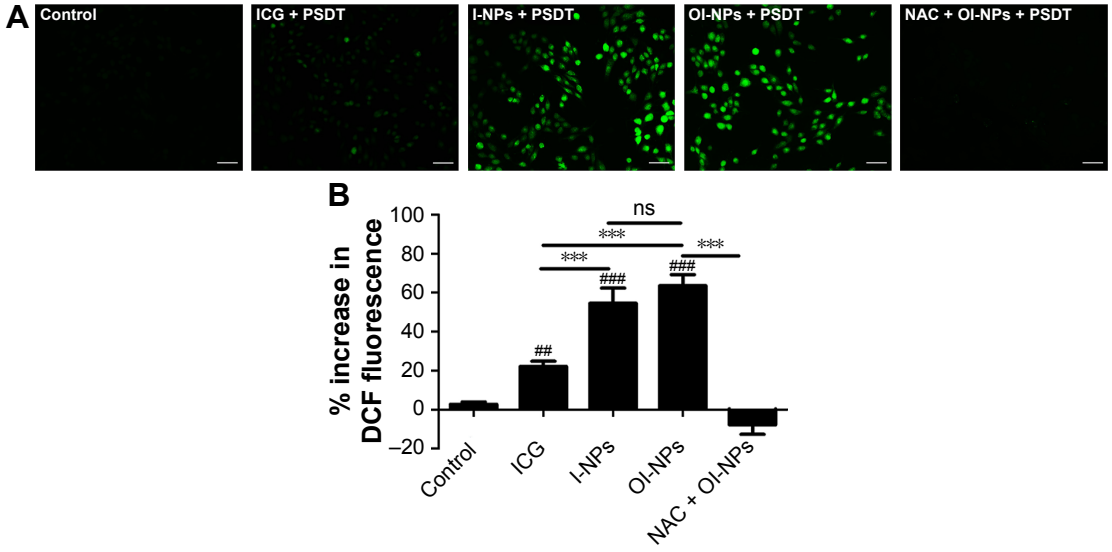

Figure 5 Intracellular ROS production determination.

Notes: MH7A cells incubated with DCFH-DA staining for ROS detection by fluorescence microscopy images (**A**) Scale bar is 50 μm. (**B**) Plot of % increase in DCF fluorescence for ICG, I-NPs, OI-NPs, and NAC plus OI-NPs incubated with MH7A cells upon exposure to laser and ultrasound (measured by fluorescence microplate reader). The data are shown as mean ± SD (n=3). $^{\#\#}P<0.01$ and $^{\#\#\#}P<0.001$ versus control group. $^{***}P<0.001$ between groups.

Abbreviations: DCF, 2′,7′-dichlorofluorescein; DCFH-DA, 2′,7′-dichlorofluorescin diacetate; ICG, indocyanine green; I-NPs, indocyanine green loaded nanoparticles; NAC, *N*-acetylcysteine; ns, no significant difference; OI-NPs, oxygen and indocyanine green loaded nanoparticles; PSDT, photodynamic and sonodynamic combination therapy; SD, standard deviation.

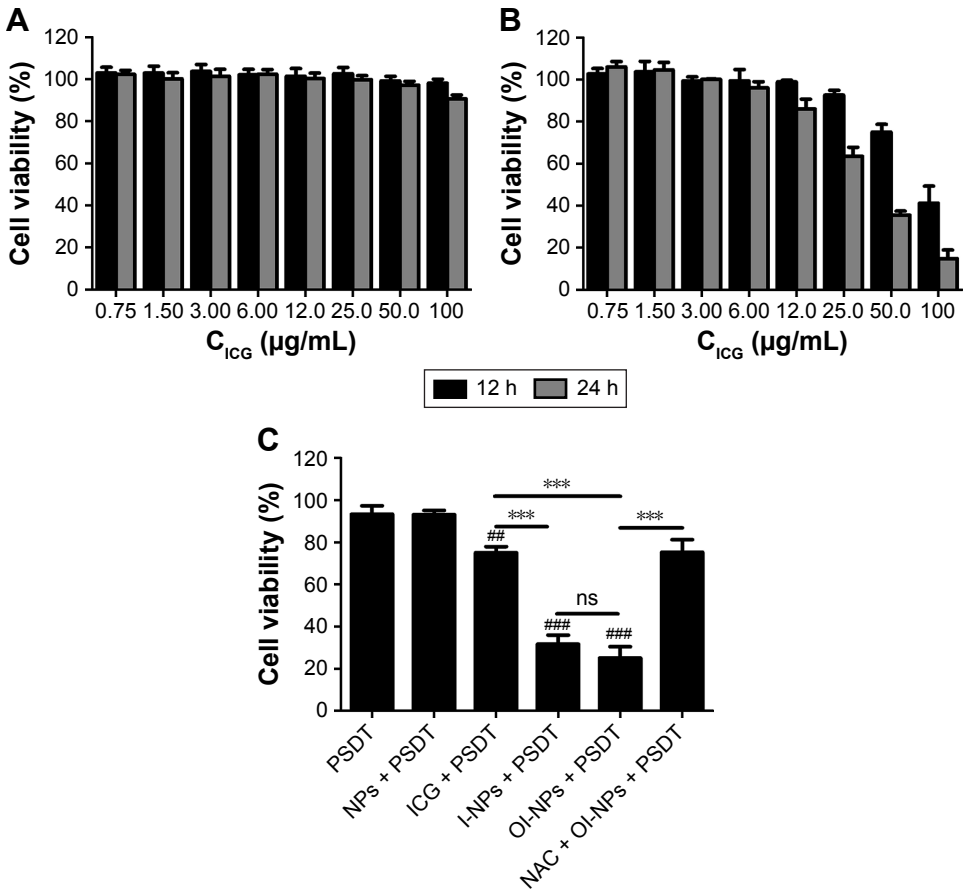

Figure 6 Cytotoxicity of free ICG (**A**) and OI-NPs (**B**) on MH7A cells determined using MTT assay. Cell viability of MH7A cells under different treatments, as determined by the MTT assay (10 μg/mL of ICG) (**C**).

Notes: The data are shown as mean ± SD (n=3). $^{\#\#}P<0.01$ and $^{\#\#\#}P<0.001$ versus control, PSDT and NP-mediated PSDT groups. $^{***}P<0.001$ between groups.

Abbreviations: ICG, indocyanine green; I-NPs, indocyanine green loaded nanoparticles; NAC, *N*-acetylcysteine; MTT, 3-(4,5-dimethylthiazol-2-yl)-2,5-diphenyltetrazoliumbromide; NP, nanoparticle; ns, no significant difference; OI-NPs, oxygen and indocyanine green loaded nanoparticles; PSDT, photodynamic and sonodynamic combination therapy; SD, standard deviation.

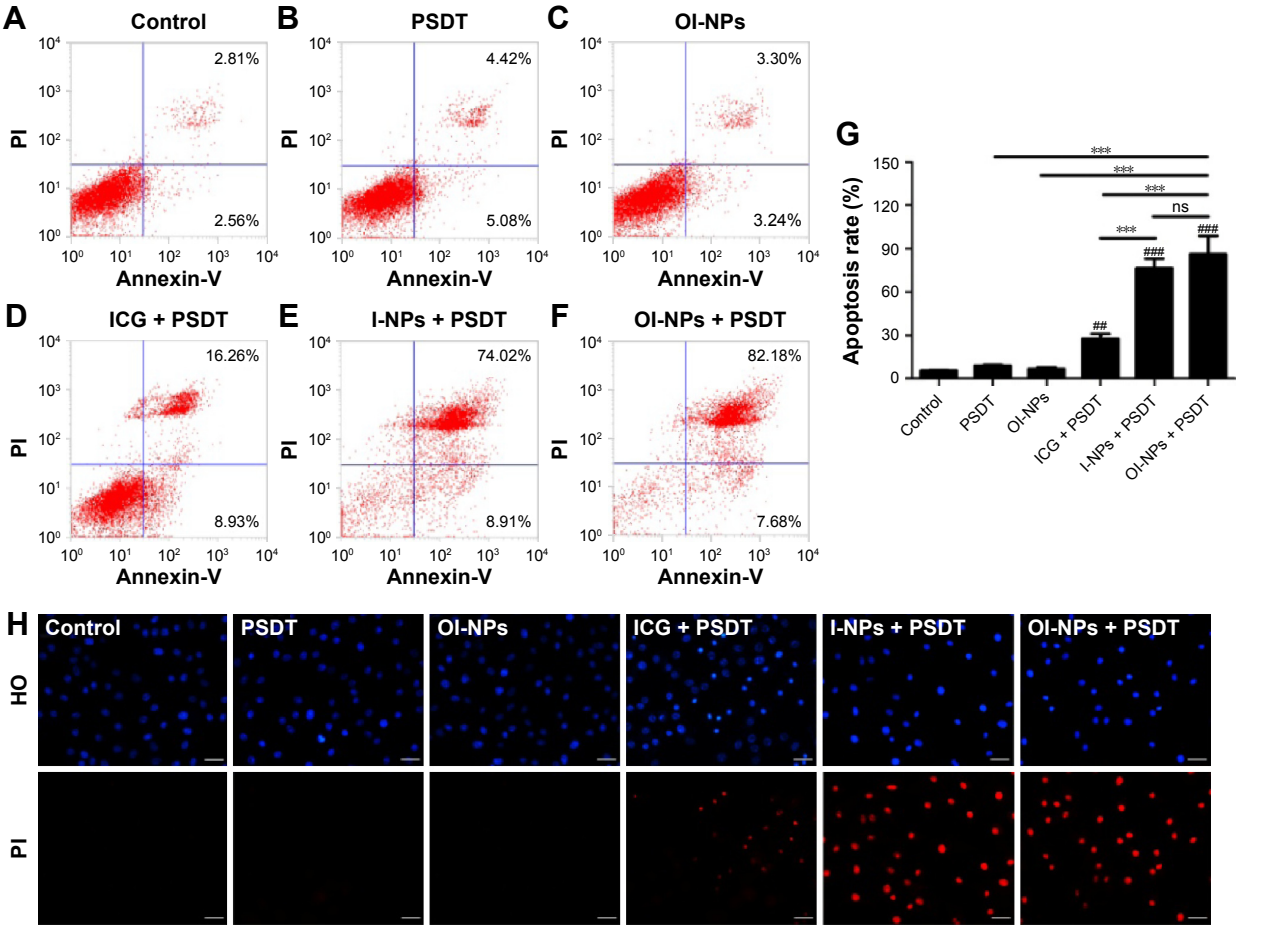

Figure 7 Apoptosis in MH7A cells detected by flow cytometry and fluorescence microscopy 24 h after different treatments.
Notes: Control (**A**); PSDT (**B**); OI-NPs (**C**); ICG + PSDT (**D**); I-NPs + PSDT (**E**); OI-NPs + PSDT (**F**); statistical results of three repeated experiments (**G**). The apoptotic nuclear and cell membrane integrity changes of MH7A cells under different treatments, as detected by HO/PI double staining using fluorescence microscopy with the same conditions (**H**). Scale bar is 50 μm. The data are shown as mean ± SD (n=3). $^{\#\#}P<0.01$ and $^{\#\#\#}P<0.001$ versus control group. $^{***}P<0.001$ between groups.
Abbreviations: ICG, indocyanine green; HO, Hoechst 33342; I-NPs, indocyanine green loaded nanoparticles; ns, no significant difference; OI-NPs, oxygen and indocyanine green loaded nanoparticles; PI, propidium iodide; PSDT, photodynamic and sonodynamic combination therapy; SD, standard deviation.

alone groups displayed circular nuclei; the chromatin was uniformly stained on HO with blue fluorescence and almost no PI red fluorescence, indicating no cell damage occurred. There was a small number of light and brighter red stained cells in ICG-mediated PSDT group, showing part of the cells was damaged. I-NP– or OI-NP–mediated PSDT group significantly increased HO and PI staining, indicating the typical apoptosis characteristics such as formation of fragment, deformed nuclei, unclear aggregates, and impairment in membrane integrity.

Discussion

Striking progress has been achieved in the management of RA in the last decades. However, some patients do not respond well to the therapeutics presently available, and some of these cases with destruction of joints are considered for synovectomy to prevent further damage of vital joint structures. PSDT is proposed in this study for the enhanced effects and reduced adverse reaction. Our results show for the first time that OI-NP–mediated PSDT is a new and promising method for killing RA synoviocytes in vitro, and ROS production is one of the underlying mechanisms in the process.

In this study, the OI-NPs were assembled with ICG, oxygen, PFP, and PLGA by a modified double emulsion method. The prepared NPs have many unique advantages: 1) Biosafety: both PLGA and ICG are Food and Drug Administration approved and have been clinically used in biological and medical applications. Besides, PFC has long been used as an artificial O_2 carrier in clinical practice.[43] 2) Stability: the stability of ICG was notably improved after it was loaded into PLGA NPs, therefore exerting long-lasting antiarthritis effect. 3) Synergistic effect: after irritated by near-infrared laser, the liquid PFP caused droplet-to-bubble transition and the NPs converted to microbubbles, while exerting

photodynamic action. The microbubbles were ruptured when exposed to low-intensity focused insonation and caused cavitation, while releasing oxygen and ICG and generating sonodynamic reaction. Our results demonstrated that the laser and ultrasound pulses effectively introduced PFP phase shift, ruptured, and effectively released oxygen (data are not shown). The effect of PDT and SDT combination therapy is coincident with previous reports, except that in our study, the process was activated in sequence by light and ultrasound.[14,16]

The cellular uptake and intracellular distribution of sensitizers is potentially important for PDT and SDT. So, we determined the uptake ability of MH7A cells for free ICG and OI-NPs. The results showed that cellular uptake of the ICG was 35% higher in the OI-NPs group than that in the free ICG group (Figure 4), which may be due to the easier cellular internalization of the ICG loaded in OI-NPs by endocytosis pathway.

The cytotoxic effect of OI-NP–mediated PSDT on MH7A cells was determined by MTT assay. The results showed that PSDT alone and blank NP-mediated PSDT group had no obvious cytotoxic effect on MH7A cells, indicating that blank NPs could not produce ROS or phase transition without ICG, even under laser and ultrasound exposure. But there was a significant increase in PSDT-mediated cytotoxicity for I-NPs or OI-NPs compared with free ICG group, which may be directly attributed to the enhanced cellular uptake of sensitizers. However, there was no significant difference between I-NP–mediated PSDT and OI-NP–mediated PSDT groups, though the ROS production in cell-free system was significantly different between the two groups (Figure 3B, $P<0.05$). The reason may be that MH7A cells were in a normal oxygen environment in the present study and the normoxic condition could provide sufficient oxygen that PSDT needed. Our follow-up experiment will further investigate the therapeutic effect of the two NPs-mediated PSDT in hypoxic environment.

Apoptosis is one of the major modes of cell death and can be induced in PDT or SDT process.[16] Many morphologic characteristics related to apoptosis, including cell shrinkage, nuclear chromatin condensation, and DNA fragmentation, have been defined clearly. To confirm whether cell apoptosis was induced, flow cytometry and HO/PI double staining were performed in our study. Figure 7A–G displays a significant increase in apoptotic cell populations after I-NP– or OI-NP–mediated PSDT, compared with other groups. Besides, Figure 7H shows the typical apoptotic morphologic changes of nucleus in I-NP- or OI-NPs-mediated PSDT group. Both the flow cytometry and the HO/PI double staining results suggest that the I-NP– or OI-NP–mediated PSDT treatment aggravates apoptosis compared to other groups.

Although the underlying mechanism involved in SDT is quite complex and unclear, many investigations have demonstrated that increased ROS production may play an important role in this process, just like in PDT. Mass ROS production can induce significant oxidative damage, which destabilizes the cell membrane system by lipid peroxidation and activates the signaling pathways that regulate cell apoptosis. So, we further determined intracellular ROS generation in cell-free system and in MH7A cells after different treatments. Our results indicated that OI-NP–mediated PSDT could generate both superoxide and hydroxyl radicals (DCFH-DA as the probe in MH7A cells) and singlet oxygen (SOSG as the probe in cell-free system). What is more, the results indicated ROS generation in MH7A cells was significantly increased in the I-NP– or OI-NP–mediated PSDT group than that in free ICG-mediated PSDT group ($P<0.001$), which may also be due to the increase in uptake of I-NPs or OI-NPs by MH7A cells. In addition, co-administration with NAC, a scavenger of ROS, significantly relieved the cell cytotoxic effect of MH7A cells induced by PSDT, suggesting ROS production may play a crucial role in OI-NP–mediated PSDT. These results suggest an oxidative stress mechanism may be involved in response to OI-NP–mediated PSDT in MH7A cells. However, blocking the ROS could not completely eliminate the cytotoxic effect in MH7A cells, which may be due to the additional mechanical damage effects during the phase transition and rupture of NPs or other unclear mechanisms involved.

Conclusion

In this study, we have successfully developed stable and synergistic OI-NPs as a favorable sensitizer and oxygen carrier for PSDT, and further study evaluated the therapeutic potential of OI-NP–mediated PSDT on RA-FLSs of MH7A cells. The results suggested that OI-NP–mediated PSDT could cause serious cell damage and evident cell apoptosis, and the potential mechanism of OI-NP–mediated PSDT may stem from the greater accumulation of ICG from OI-NPs by MH7A cells and increased intracellular ROS generation. This study may provide a new strategy for the treatment of RA and develop a model of theranostic application through phase-transition NP-mediated PSDT in the future.

Acknowledgments

This work was supported by the National Natural Science Foundation of China (Grant numbers: 81572558, 81372799)

and Chongqing Postgraduate Research Innovation Project (Grant numbers: CYS 15139, CYS 16127).

Disclosure

The authors report no conflicts of interest in this work.

References

1. MclnnesIB, Schett G. The pathogenesis of rheumatoid arthritis. *N Engl J Med*. 2011;365(23):2205–2219.
2. Choy E. Understanding the dynamics: pathways involved in the pathogenesis of rheumatoid arthritis. *Rheumatology (Oxford)*. 2012; 51(Suppl 5):v3–v11.
3. Firestein GS. Evolving concepts of rheumatoid arthritis. *Nature*. 2003; 423(6937):356–361.
4. Bartok B, Firestein GS. Fibroblast-like synoviocytes: key effector cells in rheumatoid arthritis. *Immunol Rev*. 2010;233(1):233–255.
5. Konisti S, Kiriakidis S, Paleolog EM. Hypoxia–a key regulator of angiogenesis and inflammation in rheumatoid arthritis. *Nat Rev Rheumatol*. 2012;8(3):153–162.
6. Boissier MC, Semerano L, Challal S, Saidenberg-Kermanac'h N, Falgarone G. Rheumatoid arthritis: from autoimmunity to synovitis and joint destruction. *J Autoimmun*. 2012;39(3):222–228.
7. Agostinis P, Berg K, Cengel KA, et al. Photodynamic therapy of cancer: an update. *CA Cancer J Clin*. 2011;61(4):250–281.
8. Gabriel D, Busso N, So A, van den Bergh H, Gurny R, Lange N. Thrombin-sensitive photodynamic agents: a novel strategy for selective synovectomy in rheumatoid arthritis. *J Control Release*. 2009;138(3): 225–234.
9. Gabriel D, Lange N, Chobaz-Peclat V, et al. Thrombin-sensitive dual fluorescence imaging and therapeutic agent for detection and treatment of synovial inflammation in murine rheumatoid arthritis. *J Control Release*. 2012;163(2):178–186.
10. Kirdaite G, Lange N, Busso N, Van Den Bergh H, Kucera P, So A. Protoporphyrin IX photodynamic therapy for synovitis. *Arthritis Rheum*. 2002;46(5):1371–1378.
11. McHale AP, Callan JF, Nomikou N, Fowley C, Callan B. Sonodynamic therapy: concept, mechanism and application to cancer treatment. *Adv Exp Med Biol*. 2016;880:429–450.
12. Costley D, Mc Ewan C, Fowley C, et al. Treating cancer with sonodynamic therapy: a review. *Int J Hyperthermia*. 2015;31(2):107–117.
13. Li Q, Liu Q, Wang P, Feng X, Wang H, Wang X. The effects of Ce6-mediated sono-photodynamic therapy on cell migration, apoptosis and autophagy in mouse mammary 4T1 cell line. *Ultrasonics*. 2014;54(4): 981–989.
14. Liu Y, Wang P, Liu Q, Wang X. Sinoporphyrin sodium triggered sono-photodynamic effects on breast cancer both in vitro and in vivo. *Ultrason Sonochem*. 2016;31:437–448.
15. Wang H, Wang X, Wang P, Zhang K, Yang S, Liu Q. Ultrasound enhances the efficacy of chlorin E6-mediated photodynamic therapy in MDA-MB-231 cells. *Ultrasound Med Biol*. 2013;39(9):1713–1724.
16. Wang P, Li C, Wang X, et al. Anti-metastatic and pro-apoptotic effects elicited by combination photodynamic therapy with sonodynamic therapy on breast cancer both in vitro and in vivo. *Ultrason Sonochem*. 2015;23: 116–127.
17. Kolarova H, Tomankova K, Bajgar R, Kolar P, Kubinek R. Photodynamic and sonodynamic treatment by phthalocyanine on cancer cell lines. *Ultrasound Med Biol*. 2009;35(8):1397–1404.
18. Tserkovsky DA, Alexandrova EN, Chalau VN, Istomin YP. Effects of combined sonodynamic and photodynamic therapies with photolon on a glioma C6 tumor model. *Exp Oncol*. 2012;34(4):332–335.
19. Sun X, Xu H, Shen J, et al. Real-time detection of intracellular reactive oxygen species and mitochondrial membrane potential in THP-1 macrophages during ultrasonic irradiation for optimal sonodynamic therapy. *Ultrason Sonochem*. 2015;22:7–14.
20. Wang J, Guo Y, Gao J, et al. Detection and comparison of reactive oxygen species (ROS) generated by chlorophyllin metal (Fe, Mg and Cu) complexes under ultrasonic and visible-light irradiation. *Ultrason Sonochem*. 2011;18(5):1028–1034.
21. Wang J, Xu M, Chen M, Jiang Z, Chen G. Study on sonodynamic activity of metallophthalocyanine sonosensitizers based on the sonochemiluminescence of MCLA. *Ultrason Sonochem*. 2012;19(2):237–242.
22. Smith BA, Gammon ST, Xiao S, et al. In vivo optical imaging of acute cell death using a near-infrared fluorescent zinc-dipicolylamine probe. *Mol Pharm*. 2011;8(2):583–590.
23. Adams KE, Ke S, Kwon S, et al. Comparison of visible and near-infrared wavelength-excitable fluorescent dyes for molecular imaging of cancer. *J Biomed Opt*. 2007;12(2):024017.
24. Landsman ML, Kwant G, Mook GA, Zijlstra WG. Light-absorbing properties, stability, and spectral stabilization of indocyanine green. *J Appl Physiol*. 1976;40(4):575–583.
25. Nomikou N, Sterrett C, Arthur C, McCaughan B, Callan JF, McHale AP. The effects of ultrasound and light on indocyanine-green-treated tumour cells and tissues. *ChemMedChem*. 2012;7(8):1465–1471.
26. Yoneya S, Saito T, Komatsu Y, Koyama I, Takahashi K, Duvoll-Young J. Binding properties of indocyanine green in human blood. *Invest Ophthalmol Vis Sci*. 1998;39(7):1286–1290.
27. Saxena V, Sadoqi M, Shao J. Degradation kinetics of indocyanine green in aqueous solution. *J Pharm Sci*. 2003;92(10):2090–2097.
28. Desmettre T, Devoisselle JM, Mordon S. Fluorescence properties and metabolic features of indocyanine green (ICG) as related to angiography. *Surv Ophthalmol*. 2000;45(1):15–27.
29. Chang S, Si T, Zhang S, Merrick MA, Cohn DE, Xu RX. Ultrasound mediated destruction of multifunctional microbubbles for image guided delivery of oxygen and drugs. *Ultrason Sonochem*. 2016;28:31–38.
30. Jian J, Liu C, Gong Y, et al. India ink incorporated multifunctional phase-transition nanodroplets for photoacoustic/ultrasound dual-modality imaging and photoacoustic effect based tumor therapy. *Theranostics*. 2014;4(10):1026–1038.
31. McEwan C, Fowley C, Nomikou N, McCaughan B, McHale AP, Callan JF. Polymeric microbubbles as delivery vehicles for sensitizers in sonodynamic therapy. *Langmuir*. 2014;30(49):14926–14930.
32. Zhang X, Zheng Y, Wang Z, et al. Methotrexate-loaded PLGA nanobubbles for ultrasound imaging and synergistic targeted therapy of residual tumor during HIFU ablation. *Biomaterials*. 2014;35(19):5148–5161.
33. Zheng C, Zheng M, Gong P, et al. Indocyanine green-loaded biodegradable tumor targeting nanoprobes for in vitro and in vivo imaging. *Biomaterials*. 2012;33(22):5603–5609.
34. Xu RX, Huang J, Xu JS, et al. Fabrication of indocyanine green encapsulated biodegradable microbubbles for structural and functional imaging of cancer. *J Biomed Opt*. 2009;14(3):034020.
35. Saxena V, Sadoqi M, Shao J. Polymeric nanoparticulate delivery system for Indocyanine green: biodistribution in healthy mice. *Int J Pharm*. 2006;308(1–2):200–204.
36. Manchanda R, Fernandez-Fernandez A, Nagesetti A, McGoron AJ. Preparation and characterization of a polymeric (PLGA) nanoparticulate drug delivery system with simultaneous incorporation of chemotherapeutic and thermo-optical agents. *Colloids Surf B Biointerfaces*. 2010; 75(1):260–267.
37. Lowe KC. Perfluorinated blood substitutes and artificial oxygen carriers. *Blood Rev*. 1999;13(3):171–184.
38. Srinivas M, Tel J, Schreibelt G, et al. PLGA-encapsulated perfluorocarbon nanoparticles for simultaneous visualization of distinct cell populations by 19F MRI. *Nanomedicine (Lond)*. 2015;10(15):2339–2348.
39. Yao Y, Zhang M, Liu T, et al. Perfluorocarbon-encapsulated PLGA-PEG emulsions as enhancement agents for highly efficient reoxygenation to cell and organism. *ACS Appl Mater Interfaces*. 2015;7(33): 18369–18378.
40. Zhao Y, Song W, Wang D, et al. Phase-Shifted PFH@PLGA/Fe3O4 nanocapsules for MRI/US imaging and photothermal therapy with near-infrared irradiation. *ACS Appl Mater Interfaces*. 2015; 7(26):14231–14242.

41. Mitra K, Melvin J, Chang S, et al. Indocyanine-green-loaded microballoons for biliary imaging in cholecystectomy. *J Biomed Opt*. 2012; 17(11):116025.
42. Ma Y, Sadoqi M, Shao J. Biodistribution of indocyanine green-loaded nanoparticles with surface modifications of PEG and folic acid. *Int J Pharm*. 2012;436(1–2):25–31.
43. Spahn DR, Kocian R. Artificial O2 carriers: status in 2005. *Curr Pharm Des*. 2005;11(31):4099–4114.